AIP Journal of Applied Physics

Three-point bending analysis of doubly clamped silicon nanowire beams; Young's modulus, initial stress, and crystal orientation

Y. E. Yaish, Y. Calahorra, O. Shtempluck, and V. Kotchetkov

Citation: Journal of Applied Physics **117**, 164311 (2015); doi: 10.1063/1.4919017
View online: http://dx.doi.org/10.1063/1.4919017
View Table of Contents: http://scitation.aip.org/content/aip/journal/jap/117/16?ver=pdfcov
Published by the AIP Publishing

JOURNAL OF APPLIED PHYSICS **117**, 164311 (2015)

Three-point bending analysis of doubly clamped silicon nanowire beams; Young's modulus, initial stress, and crystal orientation

Y. E. Yaish,[a] Y. Calahorra, O. Shtempluck, and V. Kotchetkov
Department of Electrical Engineering, Technion, Haifa 32000, Israel

(Received 1 January 2015; accepted 14 April 2015; published online 30 April 2015)

A non-linear model is introduced describing the force-deflection relation of doubly clamped beams, including initial stress. Several approximations for the exact model are developed and compared, revealing the importance of considering the initial stress during 3-point bending measurements analysis. A novel approximation is found to be better than others, and both the exact model and this approximation are in perfect agreement with finite element simulations. A brief experimental example of silicon nanowires is presented in which the Young's modulus, the initial stress, and the crystallographic growth orientation are extracted by 3-point bending analysis. © *2015 AIP Publishing LLC*. [http://dx.doi.org/10.1063/1.4919017]

I. INTRODUCTION

Many materials can be grown or fabricated to the shape of beams or nanowires. Such nanostructures are considered building blocks of future electronics, optics, and mechanics.[1–3] Various applications have been suggested and realized, such as fast electrical devices, light emitting diodes, single mode lasers, nanoelectromechanical systems (NEMS), and chemical and biological sensors.[4–13] Among the various nanowires grown from different materials, an attractive candidate is silicon nanowire (SiNW), whose mechanical properties are of great importance, for example, for NEMS and piezoresistive applications.[14] Understanding the mechanical properties of nanowires in general, and of SiNWs in particular, and the ability to control and quantify them, are of crucial importance for successful realization of such applications.

The ability to measure and modify the initial stress of electronic devices (sometimes referred to as residual tension, when dealing with post-processing effects) is an important and exciting possibility due to piezoresistive effects that can improve device properties. Indeed, strain engineering is increasingly used nowadays in the microelectronics industry,[15–17] and SiNWs are promising candidates. SiNWs have, for example, unusually high piezoresistive coefficients, as reported by He and Yang,[14] thus increasing the motivation for NW strain engineering applications.

To quantify the mechanical properties of nanowires, different measurement schemes have been introduced, including scanning electron microscopy (SEM) and transmission electron microscopy (TEM) methods,[18–24] nanoindentation techniques,[25,26] dynamic resonance measurements,[8,27] and atomic force microscopy (AFM) based 3-point bending experimrnts.[27–38] The advantage of the last two methods is that they enable measurements to be performed directly on fabricated mechanical devices, such as doubly clamped beams, thus taking process influences into consideration.

A doubly clamped beam may develop residual stresses during clamping or due to subsequent processing, or it may accommodate inherent initial stresses, all of which may affect its electronic properties. In this study, a new approach to the analysis of 3-point bending measurements of doubly clamped beams is introduced that takes initial stress into account. In addition to the analytical solution, several approximations are derived and compared, and one approximation is found to be very accurate and easy to employ. An example of this analysis is given for doubly clamped SiNW beams before and after rapid thermal annealing (RTA) treatment. Results show that RTA modifies the initial stress along the beam and crystal growth orientation of the studied wires may be extracted using the proposed analysis.

II. THEORETICAL ANALYSIS

Studies reported in current literature focus predominantly on the extraction of the Young's modulus of nanobeams. Results obtained for SiNWs are still inconclusive, and a widely accepted model for the Young's modulus of SiNWs has yet to be introduced. For NWs made of different materials, values similar to bulk values have been reported,[27,30,32,36,37] as well as values that increase[33,35] as the NW diameter decreases and values that decrease[39,40] as the thickness of Si nanocantilevers decreases.

Atomistic simulations fail to explain such variations in the Young's modulus of mechanical systems with characteristic thicknesses greater than several nm.[41–43] Such effects are usually attributed to surface elasticity[33,44] and NW composite structure.[39,45,46] The composite structure of SiNWs consists of a Si core and a SiO_2 shell. The flexural rigidity of a core-shell system is given by[45]

$$E_{eff}I_{eff} = E_{core}I_{core} + E_{shell}I_{shell}, \tag{1}$$

where I is the area moment of inertia which is $\pi r^4/4$ for a cylinder and $\pi(r_{outer}^4 - r_{inner}^4)/4$ for a cylindrical shell, and E is the relevant Young's modulus. Thus, the following relationship is found for the effective modulus[46]

[a]yuvaly@ee.technion.ac.il

$$E_{eff} = E_{shell} + (E_{core} - E_{shell})\left(\frac{d_{core}}{d_{total}}\right)^4, \quad (2)$$

where $E_{shell} = 70\,\text{GPa}$,[36] and d_{core} and d_{total} are, respectively, the NW core diameter and total diameter.

In continuous mechanics, the basic differential equation that determines the equilibrium position of a doubly clamped beam of length L subjected to point force, $F\hat{z}$, at its center is given by[47]

$$EI\frac{\partial^4 u}{\partial x^4} - T\frac{\partial^2 u}{\partial x^2} = \frac{F}{2}\left(-\delta(x) + 2\delta(x - L/2) - \delta(x - L)\right), \quad (3)$$

where $u(x)$ is the transversal displacement in the z direction and x is the beam longitudinal axis. The first term originates from the beam bending and the second term is attributed to initial tension and stretching along the axial direction of the beam. The overall tension is given by

$$T = T_0 + \frac{ES}{2L_{relx}}\int_0^L \left(\frac{\partial u}{\partial x}\right)^2 dx, \quad (4)$$

where T_0 is the residual or initial tension, L_{relx} is the relaxed length of the beam (with zero strain), and L is the distance between the beam's two clamping points. The relaxed beam length may be smaller or larger than L, depending on whether the initial tension is positive or negative, respectively. A simple calculation shows, however, that $L_{relx}/L = E/(E + \sigma_0)$, where $\sigma_0 = T_0/S$, and $S = \pi R^2$ is the circular beam cross section. In many experiments conducted using the 3-point bending method, the Young's modulus is significantly larger than σ_0 (by at least several hundred Pa), thus rendering the following approximation, $L_{relx} \approx L$, completely justified.

Integrating Eq. (3) with respect to x, assuming $T > 0$ for the forthcoming analysis, yields

$$L_0^2\frac{\partial^3 u}{\partial x^3} - \frac{\partial u}{\partial x} = -\frac{F}{2T}, \quad (5)$$

where $L_0^2 = EI/T$. Using the common boundary conditions for doubly clamped beams $(u(0) = u(L) = u'(0) = u'(L) = 0)$, the following analytical solution is obtained:

$$u(x) = \frac{F}{2T}\frac{1}{\cosh(L/4L_0)}\left(x\cosh(L/4L_0) - L_0\left(\sinh(L/4L_0) - \sinh\left((L - 4x)/4L_0\right)\right)\right). \quad (6)$$

At $x = L/2$, Eq. (6) reduces to

$$u(L/2) = \frac{F}{2T}\frac{1}{\cosh(L/4L_0)}\times\left(L/2\cosh(L/4L_0) - 2L_0\sinh(L/4L_0)\right). \quad (7)$$

Plugging Eq. (6) back into Eq. (4) results in

$$T = T_0 + \frac{ESF^2}{16T^2}\frac{1}{\cosh^2(L/4L_0)}\times\left(2 + \cosh(L/2L_0) - 6\frac{L_0}{L}\sinh(L/2L_0)\right). \quad (8)$$

For small deflections and low T_0, Eq. (7) may be expanded by powers of T to obtain

$$u(L/2) \approx \frac{FL^3}{192EI}\left(1 - \frac{L^2T}{40EI} + \frac{17}{26880}\left(\frac{L^2T}{EI}\right)^2\right). \quad (9)$$

Two main observations can be made from this last equation. First, we see that the relevant small parameter of the expansion is $\alpha = \frac{L^2T}{EI} = \left(\frac{L}{L_0}\right)^2$, which is a measure of the ratio between the stretching and bending contributions to the beam deflection. Second, rewriting Eq. (9) as

$$F_{ext} \equiv F = \frac{192EI}{L^3}u(L/2)f(\alpha) \quad (10)$$

yields the well known linear approximation of beam deflections for $f(\alpha) = 1$. This relationship is commonly used in the literature to extract the beam's Young's modulus.[30,33–36] The two main shortcomings of the linear model is that it is applicable only for deflections smaller than the beam's thickness and that it is extremely sensitive to initial stress, as discussed below. For deflections that are greater or comparable to the beam's thickness (referred to as large deflections), tensile forces due to stretching become significant and the force-deflection (F-D) curve deviates substantially from linearity. This can be described by adding a cubic term to the equation, resulting in a rough approximation of the complete model.[29]

It was only in 2006 that Heidelberg *et al.*[29] introduced a model that consisted of a Padé approximation of the analytical solution of the beam equation. This model, which produced a F-D curve for the entire range of deflections, was further used only in subsequent works by co-workers.[32,37] In this study, we follow Heidelberg's analysis and introduce an exact set of equations and relevant approximations for the case of initial stresses.

The first step is to find $f(\alpha)$. Plugging Eq. (7) into Eq. (10) and eliminating F results in

$$f(\alpha) = \frac{\alpha}{48 - \frac{192\tanh\left(\sqrt{\alpha}/4\right)}{\sqrt{\alpha}}}. \quad (11)$$

Inserting Eqs. (10) and (11) into Eq. (8) yields

$$\left(\alpha - \frac{L^2T_0}{EI}\right)\frac{\cosh^2\left(\sqrt{\alpha}/4\right)}{2 + \cosh\left(\sqrt{\alpha}/2\right) - 6\sinh\left(\sqrt{\alpha}/2\right)/\sqrt{\alpha}}\times\left(1 - 4\tanh\left(\sqrt{\alpha}/4\right)/\sqrt{\alpha}\right)^2 = \frac{S}{I}u^2(L/2). \quad (12)$$

The set of Eqs. (10) and (12) may be solved self-consistently, for a given set of F-D data, to determine the two unknowns, E, and T_0. The convergence of this procedure is very slow, and if the residual tension is negative, which is quite common, the results obtained might be erroneous, depending on the initial guess for the two unknown variables. To facilitate this procedure and to develop better intuition of the beam deflections, different approximations should be applied and tested.

If $\alpha_0 = L^2T_0/EI < 1$ and $\epsilon = u^2S/I < 1$, Eq. (12) may be expanded by powers of T_0 and u to obtain

$$\left(\alpha - \frac{L^2T_0}{EI}\right)\frac{5}{12} \simeq \frac{S}{I}u^2 = \epsilon. \tag{13}$$

Solving this equation for α yields

$$\alpha \simeq \frac{12}{5}\epsilon + \frac{L^2T_0}{EI}. \tag{14}$$

When the residual tension increases, and u is very small, the following condition must be fulfilled in order for the left side of Eq. (12) to be very small:

$$\alpha \to \frac{L^2T_0}{EI}. \tag{15}$$

When u increases and its contribution to T becomes more significant, α increases as well, and the term L^2T_0/EI in Eq. (12) becomes less important. In this situation, both a high and a low limits are obtained[29]

$$\alpha = \begin{cases} \frac{12}{5}\epsilon - \frac{3}{875}\epsilon^2, & \epsilon < 1 \\ 2\epsilon, & \epsilon > 1. \end{cases} \tag{16}$$

In the absence of residual tension, Heidelberg *et al.*[29] performed a Padé approximation for α, based on the two limiting values presented in Eq. (16). When $T_0 \neq 0$, the results of Eqs. (14)–(16) may be combined, yielding the following approximation for α:

$$\alpha \simeq \frac{L^2T_0}{EI} + \frac{6\epsilon(140+\epsilon)}{350+3\epsilon} \equiv \alpha_{app}. \tag{17}$$

To obtain the leading terms in the expansion of the F-D curve, we use the approximation for $f(\alpha)$ for small α

$$f(\alpha) \approx 1 + \frac{\alpha}{40} - \frac{\alpha^2}{134400} \tag{18}$$

together with Eq. (17) to find the following relationship:

$$f(\alpha) \approx 1 + \frac{1}{40}\frac{L^2T_0}{EI} + \frac{3}{50}\epsilon - \frac{1}{134400}\left(\frac{L^2T_0}{EI}\right)^2 - \frac{9}{70000}\epsilon^2 - \frac{1}{28000}\frac{L^2T_0}{EI}\epsilon. \tag{19}$$

Equation (19) presents the exact analytical solution, based on the Taylor expansion, of the set of Eqs. (10) and (12) up to the second order terms in the series. For an F-D analysis that is based on the linear approximation, Eq. (10) (the leading term) becomes

$$F = \frac{192EI}{L^3}u(L/2)\left(1 + \frac{1}{40}\frac{L^2T_0}{EI}\right). \tag{20}$$

Unlike the negligible contribution of T_0 to the beam length ($\sigma_0/E \ll 1$, thus $L \approx L_{relx}$), the term

$$\frac{L^2T_0}{EI} = \frac{\sigma_0}{E}\frac{4L^2}{R^2} \tag{21}$$

includes the multiplication factor $(2L/R)^2$, which increases as the aspect ratio of beam length to beam radius increases. For typical beams, such as SiNWs, lengths are in the several microns range, and radii are in the tens of nanometers range: thus, the squared aspect ratio contributes a factor of 10^3–10^4 to the original $\sigma_0/E \ll 1$ ratio. Taken together, this term in Eq. (20) ($b = L^2T_0/40EI$) may be of the order 1. For example, for a NW beam of $L = 1\,\mu$m, $R = 20$ nm, $E = 200$ GPa, and $\sigma_0 = 400$ MPa, $b = 0.5$. If the Young's modulus is extracted using the linear approximation with $f(\alpha) = 1$ (Eq. (10)), the resulting $E_{measured}$ will be (up to the first order in T_0)

$$E_{measured} = E\left(1 + \frac{1}{40}\frac{L^2T_0}{EI}\right). \tag{22}$$

This incorrect interpretation of the F-D data may lead to substantial errors in the calculation of the NW's Young's modulus, and may result in the increase or decrease of E, depending on whether T_0 is positive (elongation) or negative (compression). In the above example, for instance, where $b = 0.5$, the calculation yields $E = 300$ GPa instead of $E = 200$ GPa. Moreover, even if we take into account the fact that the slope of the F-D curve within the linear regime depends on E and T_0, it is impossible to determine these two parameters uniquely from the linear part alone. The linear behavior of the F-D curve may extend more than is typical for the stress-free case. Quantitatively, in the linear regime, u satisfies the following condition:

$$\frac{3}{50}\frac{S}{I}u^2 \ll \mathrm{Max}\left(1, \frac{1}{40}\frac{L^2T_0}{EI}\right), \tag{23}$$

which reduces to

$$\begin{aligned} &u \ll 2R \quad \text{for} \quad 1 > \frac{1}{10}\left(\frac{L}{R}\right)^2\frac{\sigma_0}{E} \\ &\text{or} \\ &\frac{u}{L} \ll \sqrt{\frac{\sigma_0}{40E}} \quad \text{for} \quad 1 < \frac{1}{10}\left(\frac{L}{R}\right)^2\frac{\sigma_0}{E}. \end{aligned} \tag{24}$$

When σ_0 is negligible and/or the beam aspect ratio is low, the linear behavior range is smaller than the NW diameter; however, for higher residual tensions and/or high NW aspect ratios, the linear range may be larger than the beam diameter. For example, for a long beam of $L = 20\,\mu$m, $R = 20$ nm, $E = 200$ GPa, and $\sigma_0 = 400$ MPa, a displacement of 100 nm is well within the linear regime.

Before examining the quality and range of validity of the previous approximations, we present a plot of $f(\alpha)$ vs. α according to Eq. (11) (Fig. 1). It is immediately obvious that $f(\alpha)$ is a simple monotonic function that easily fits a polynomial function. The best fit (red line in Fig. 1) was restricted to the format $1 + a\alpha + b\alpha^2$ and was found to be

$$f_{app}(\alpha) = 1 + 2.412 \cdot 10^{-2}\alpha - 1.407 \cdot 10^{-6}\alpha^2. \tag{25}$$

As will be discussed later, this approximation proves very useful for a broad range of beam deflections.

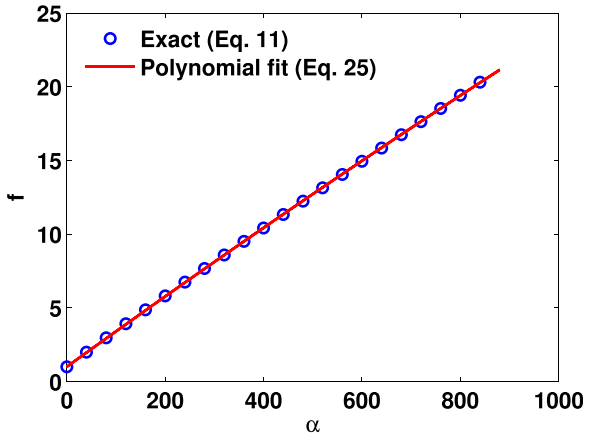

FIG. 1. $f(\alpha)$ vs. α. Blue circles represent the exact function according to Eq. (11), while the red line represents the best fit according to Eq. (25).

III. APPROXIMATE SOLUTIONS

To evaluate the various approximations correctly, we choose NW beams with parameter values (length, radius, Young's modulus, and initial tension) similar to those of a typical SiNW, and solve Eq. (12) to produce α_{exact} for a given displacement, u. Then, we evaluate $f(\alpha)$ according to Eq. (11) and produce theoretical force-displacement data which correspond to the parameters we used. Fig. 2 presents a plot of $(\alpha_{app} - \alpha_{exact})/\alpha_{exact}$ as a function of u for a NW of $L = 1\,\mu$m, $R = 20$ nm, $E = 190$ GPa, for two residual stresses, $\sigma_0 = 0$ MPa and 500 MPa. As is evident from the graph, the relative deviation of α_{app} from the exact value is less than 2% for both initial stresses, over the entire range of u, which extends to 10 times the beam radius. This result was confirmed for several beam dimensions, Young's modulus, and initial stresses, and justifies the use of Eq. (17) as an excellent approximation for α, even in cases where $\sigma_0 \neq 0$.

Knowing that α_{app} is an excellent approximation, we may proceed to examine several approximations of the theoretical F-D data that utilize different forms of $f(\alpha_{app})$ within the basic structure of Eq. (10). The first approximation (f_1) is described by Eq. (19) up to the first order of T_0 and ϵ. The second (f_2) is described by the full expression of Eq. (19), the third (f_3) by Eq. (18), and the fourth and last approximation (f_4), is described by Eq. (25). Figs. 3(a) and 3(b) present the exact force-displacement curve and the four discussed approximations for $\sigma_0 = 0$ MPa and 500 MPa, respectively. Figs. 4(a) and 4(b) present the relative deviations of these four approximations from the exact F-D data, i.e., $(F_i(u) - F_{exact}(u))/F_{exact}(u)$, for the two initial stresses. The quality and range of validity of each approximation can be deduced from these four graphs. The first three approximations (f_1, f_2, and f_3), which originate from the Taylor expansion, are very similar, although the range of validity of f_3 is larger than that of f_1 and f_2, since the expansion in α_{app} contains higher powers of T_0 and ϵ. For displacements smaller than $4R$, $3R$, and $2R$, the relative error is less than 2% for approximations f_3, f_2, and f_1, respectively. However, the relative error for approximation f_4 is less than 2% for the entire range of u, which extends to $10R$. This observation will play an important role in the correct extraction of the initial stress and the Young's modulus from real, experimental F-D data.

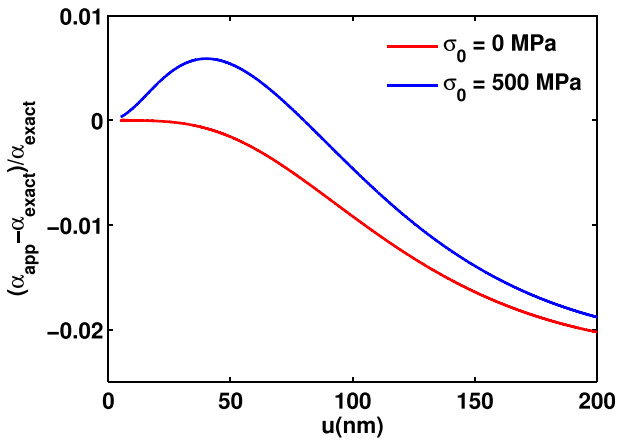

FIG. 2. Relative difference between α_{app} and α_{exact} vs. u, for $\sigma_0 = 0$ MPa and 500 MPa. The solution of Eq. (12) is α_{exact}, and α_{app} is given by Eq. (17).

The range of validity of each approximation can be derived as follows. If we expand $f(\alpha)$ up to the third power of α, we obtain the following relationship:

$$f(\alpha) \approx 1 + \frac{\alpha}{40} - \frac{\alpha^2}{134400} + \frac{\alpha^3}{48384000}. \tag{26}$$

Equation (18) is justified as long as the quadratic term in α in Eq. (26) is greater than the cubic term, i.e., $\alpha < 360$. This condition implies the two following constraints:

$$\frac{\sigma_0}{E}\left(\frac{L}{R}\right)^2 < 100 \tag{27}$$

and

$$\frac{u}{R} < 6. \tag{28}$$

For $\sigma_0 \approx 500$ MPa and $E \approx 200$ GPa, the first condition translates to $L/R < 200$, which is satisfied by the example we tested, namely, $L/R = 1000\,\text{nm}/20\,\text{nm} = 50$. The second requirement is in good agreement with the results presented in Figs. 3 and 4 for approximations f_1, f_2, and f_3. The fourth approximation, f_4, is based on a different expansion of $f(\alpha)$, as described by Eq. (25). This polynomial fit is accurate (over 97%) up to $\alpha = 1000$, which implies that

$$\frac{\sigma_0}{E}\left(\frac{L}{R}\right)^2 \leq 250 \tag{29}$$

and

$$\frac{u}{R} \leq 10. \tag{30}$$

Both conditions are fulfilled in our example and indeed, for $R = 20$ nm, the validity range of this approximation is much broader than for the other approximations and extends up to $u \leq 200$ nm, as evident from Figs. 3 and 4.

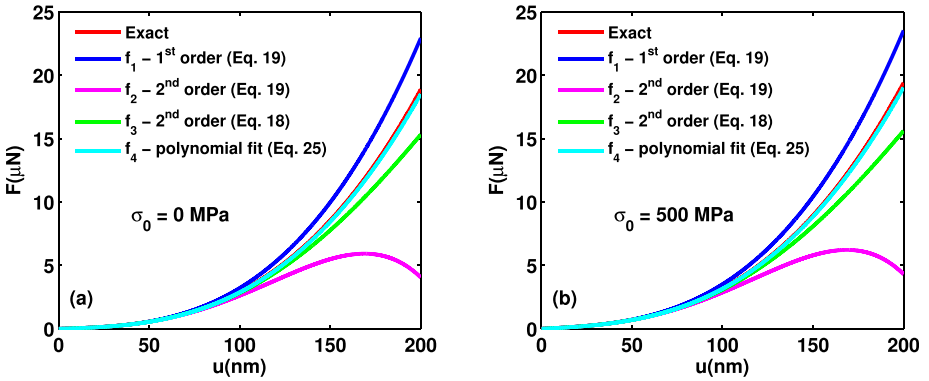

FIG. 3. The external force, F, vs. the displacement, u, of the exact solution and the four mentioned approximations (a) for zero residual stress, and (b) for a 500 MPa residual stress.

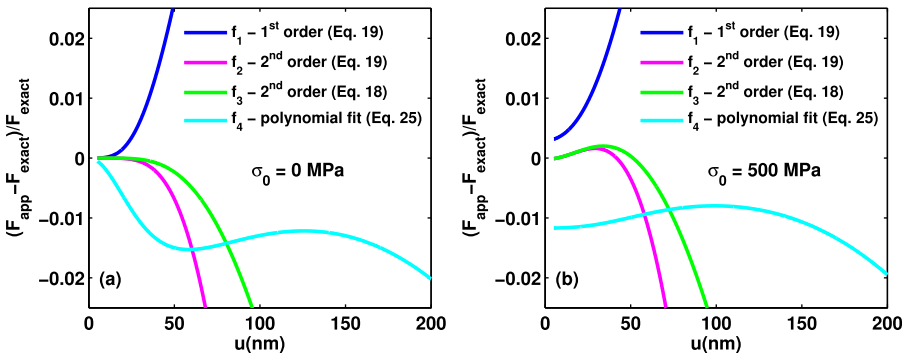

FIG. 4. The relative error of the external force, $(F_{app} - F_{exact})/F_{exact}$, vs. the displacement, u, for the four mentioned approximations (a) for zero residual stress and (b) for a 500 MPa residual stress.

IV. COMPRESSIVE RESIDUAL STRESS

So far, we have discussed the scenario of positive residual tension, $T_0 > 0$, which corresponds to beam elongation. However, to enhance the device's electrical performance, or as a consequence of the fabrication process, the beam is often under compression, and $T_0 < 0$. In such circumstances, the Euler-Bernoulli beam equation, and the resulting solutions, should be modified. For small displacements with negative initial tension, the overall tension will be negative as well. If we define $T_{new} = -T > 0$, Eq. (5) becomes

$$L_{0new}^2 \frac{\partial^3 u}{\partial x^3} + \frac{\partial u}{\partial x} = -\frac{F}{2T_{new}}, \tag{31}$$

where $L_{0new}^2 = EI/T_{new}$. The analytical solution for this equation is

$$u(x) = -\frac{F}{2T_{new}}(x - L_{0new}\sinh(x/L_{0new}) + L_0(\cos(x/L_{0new}) - 1)\tan(L/4L_{0new})) \tag{32}$$

and for $x = L/2$ we obtain

$$u(L/2) = -\frac{F}{2T_{new}}\left(\frac{L}{2} - L_{0new}\sinh(L/2L_{0new}) + L_0(\cos(L/2L_{0new}) - 1)\tan(L/4L_{0new})\right), \tag{33}$$

which reduces to

$$u(L/2) = -\frac{F}{2T_{new}}\frac{1}{\cos(L/4L_{0new})} \times (L/2\cos(L/4L_{0new}) - 2L_{0new}\sin(L/4L_{0new})). \tag{34}$$

If we recall that $L_0^2 = EI/T = -EI/T_{new} = -L_{0new}^2$, then $L_0 = \imath L_{0new}$ (taking the positive root) and the following relationships hold true:

$$\begin{aligned} \cosh(\imath z) &= \cos(z) \\ \sinh(\imath z) &= \imath\sin(z) \\ \cosh(L/4L_0) &= \cosh(-\imath L/4L_{0new}) = \cos(L/4L_{0new}) \\ \sinh(L/4L_0) &= \sinh(-\imath L/4L_{0new}) = -\imath\sin(L/4L_{0new}). \end{aligned} \tag{35}$$

Plugging Eq. (35) into Eq. (34) yields

$$u(L/2) = \frac{F}{2T}\frac{1}{\cosh(L/4L_0)} \times (L/2\cosh(L/4L_0) - 2\mathrm{sign}(T)L_0\sinh(L/4L_0)), \tag{36}$$

which has the same form as Eq. (7).

As before, u depends on T_{new}, which is unknown. Following the same procedure as presented previously

$$T = -T_{0new} + \frac{ES}{2L}\int_0^L \left(\frac{\partial u}{\partial x}\right)^2 dx \tag{37}$$

and when $T_{0new} > 0$, we obtain

$$T = -T_{0new} + \frac{ESF^2}{16T^2}\frac{1}{\cos^2(L/4L_{0new})} \times \left(2 + \cos(L/2L_{0new}) - 6\frac{L_{0new}}{L}\sin(L/2L_{0new})\right). \tag{38}$$

This solution may also be written

$$T = T_0 + \frac{ESF^2}{16T^2}\frac{1}{\cosh^2(L/4L_0)} \times \left(2 + \cosh(L/2L_0) - 6\mathrm{sign}(T)\frac{L_0}{L}\sinh(L/2L_0)\right), \tag{39}$$

which is identical to Eq. (8). When the initial tension is small, and for small displacements, the resulting tension is small, and the solution may be expanded for u (Eq. (33)) by powers of T_{new}, resulting in

$$u(L/2) \approx \frac{FL^3}{192EI}\left(1+\frac{L^2T_{new}}{40EI}+\frac{17}{26880}\left(\frac{L^2T_{new}}{EI}\right)^2\right), \quad (40)$$

which again has the same form as Eq. (9) if one replaces $T_{new} \rightarrow -T$. As expected, the expansion is by powers of $\alpha_{new}=\frac{L^2T_{new}}{EI}=\left(\frac{L}{L_{0new}}\right)^2$, and after rewriting the last equation, we find that the external force can be expressed as follows:

$$F_{ext}=\frac{192EI}{L^3}u(L/2)f(\alpha_{new}). \quad (41)$$

Plugging u from Eq. (33) into Eq. (41) eliminates $F_{ext}=F$ and results in a final equation for $f(\alpha_{new})$

$$f(\alpha_{new})=\frac{-\alpha_{new}}{48-\frac{192\tan\left(\sqrt{\alpha_{new}}/4\right)}{\sqrt{\alpha_{new}}}}. \quad (42)$$

If we recall that

$$\alpha=\left(\frac{L}{L_0}\right)^2=-\left(\frac{L}{L_{0new}}\right)^2=-\alpha_{new} \quad (43)$$

and use the following relationship:

$$\frac{\tanh\left(\sqrt{\alpha}/4\right)}{\sqrt{\alpha}}=\frac{\tanh\left(\imath\sqrt{\alpha_{new}}/4\right)}{\imath\sqrt{\alpha_{new}}}=\frac{\imath\tanh\left(\sqrt{\alpha_{new}}/4\right)}{\imath\sqrt{\alpha_{new}}}=\frac{\tan\left(\sqrt{\alpha_{new}}/4\right)}{\sqrt{\alpha_{new}}}, \quad (44)$$

we find that

$$f(\alpha_{new})=\frac{-\alpha_{new}}{48-\frac{192\tan\left(\sqrt{\alpha_{new}}/4\right)}{\sqrt{\alpha_{new}}}}=\frac{\alpha}{48-\frac{192\tanh\left(\sqrt{\alpha}/4\right)}{\sqrt{\alpha}}}=f(\alpha), \quad (45)$$

which is the same as Eq. (11) for $f(\alpha)$. Now we can go back and plug Eqs. (41) and (42) into Eq. (38), and obtain

$$\left(-\alpha_{new}+\frac{L^2T_{0new}}{EI}\right)\times\frac{\cos^2\left(\sqrt{\alpha_{new}}/4\right)}{2+\cos\left(\sqrt{\alpha_{new}}/2\right)-6\sin\left(\sqrt{\alpha_{new}}/2\right)/\sqrt{\alpha_{new}}}\times\left(1-4\tan\left(\sqrt{\alpha_{new}}/4\right)/\sqrt{\alpha_{new}}\right)^2=\frac{S}{I}u^2(L/2). \quad (46)$$

This equation is identical to Eq. (12) following the usual transformation from α_{new} to α according to Eqs. (43), (35), and (44). Indeed, this result is of fundamental importance. It tells us that in our self-consistent procedure, in which we numerically solve the set of Eqs. (10) and (12) for $\alpha > 0$, or Eqs. (41) and (46) for $\alpha < 0$, we may choose one single set of equations for both positive and negative stresses, and that a self consistent solution can be found. This equivalence between positive and negative tensions holds true also for the four approximations discussed earlier. For small $L^2T_{0new}/EI < 1$, and for $\epsilon = u^2S/I < 1$, Eq. (46) may be expanded by powers of α_{new}, leading to

$$\left(-\alpha_{new}+\frac{L^2T_{0new}}{EI}\right)\left(\frac{5}{12}-\frac{\alpha_{new}}{4032}-\frac{\alpha_{new}^2}{1128960}\right)\simeq\frac{S}{I}u^2=\epsilon. \quad (47)$$

Or, if we wish to keep only the smallest terms

$$\left(-\alpha_{new}+\frac{L^2T_{0new}}{EI}\right)\frac{5}{12}\simeq\frac{S}{I}u^2=\epsilon. \quad (48)$$

This equation leads to

$$-\alpha_{new}\simeq\frac{12}{5}\frac{S}{I}u^2-\frac{L^2T_{0new}}{EI}=\frac{12}{5}\frac{S}{I}u^2+\frac{L^2T_0}{EI}\simeq\alpha, \quad (49)$$

which is the same result as was found previously for positive tensions, i.e., Eq. (14). An increase in u brings about an increase in total tension, as well as similar increases in α, as we discussed above. Therefore, the same Padé approximation will hold true for negative residual tensions as well, and the final approximation for α will be the same as Eq. (17), i.e.,

$$-\alpha_{new}\simeq\frac{L^2T_0}{EI}+\frac{6\epsilon(140+\epsilon)}{350+3\epsilon}\simeq\alpha. \quad (50)$$

Similarly, the expansion of $f(\alpha_{new})$ for small α_{new} will be as follows:

$$f(\alpha_{new})\approx 1-\frac{\alpha_{new}}{40}-\frac{\alpha_{new}^2}{134\,400}, \quad (51)$$

which is the same as that found previously for $\alpha_{new} \rightarrow -\alpha$ (Eq. (18)). The same approximations can, therefore, be used for the force-displacement data and for f_1–f_4, for both compression and elongation stresses.

V. DISCUSSION

Unlike the theoretical procedure discussed so far, in real experiments the Young's modulus and the residual tension of a deflected beam are unknown and must be determined from the F-D data using one of several possible methods. The first method is based on solving the set of Eqs. (10) and (12) self consistently, but the convergence according to this method is very slow and if the initial guess of the two unknowns is far from the correct values, an incorrect solution for both E and T_0 may be obtained. Alternatively, the various approximations mentioned previously may be used to find the two variables. The difficulty with this approach arises from the fact that some of these approximations are very sensitive to the range of deflections for which the experimental data is being fitted. Unfortunately, if the fitted data is beyond the range of validity of the given approximations, excellent

agreement may be found between the data and the theoretical curves, while the resulting E and T_0 may be totally incorrect. This problem may explain part of the large variance in the Young's moduli of various nanobeams obtained by some researchers.

To examine this discrepancy, we decided to use approximations f_1–f_4 and study their extracted E and T_0 for different deflection fitting ranges. The results of this analysis are plotted in Figs. 5(a) and 5(b), for the four approximations used. The extracted initial tension and Young's modulus were found by fitting each approximation, from zero deflection until a given value of u/R, with the correct theoretical F-D data as calculated according to Eqs. (12) and (10), for initial stress of $\sigma_0 = 500$ MPa, and Young's modulus of $E = 190$ GPa. As is evident from the graphs, the relative errors for approximations f_1–f_3, δE, and δT_0 are small for narrow fitting ranges, but increase quite rapidly when the fitting ranges approach $5R$. Approximation f_4, however, which is based on Eq. (25), remains very accurate throughout the entire fitting range, with a relative error of less than 2%. This analysis was tested for different F-D curves, including negative residual tensions, and the observed results are in good agreement with the results presented in Figs. 4(a) and 4(b). Thus, approximation f_4 is an excellent approximation, it yields E and T_0 very rapidly and with great accuracy, and it is not subject to large errors as a result of a non-optimal fitting range. Moreover, after extracting E and T_0 from this approximation, these values may be used as initial guesses for the self-consistent procedure. In such circumstances, the method converges very rapidly (a few iterations) and the relative errors of the extracted E and T_0 are less than 0.1% of their theoretical values.

It is worth comparing our results with those obtained using the most common model used so far in the literature for extracting both E and σ_0. The model in question is based on the principle of virtual work, which utilizes the variational method to find the minimum potential energy of a given structure. An example of such a procedure was given by Senturia,[48] who derived the F-D curve for a suspended rectangular beam that included residual tension, using a simple analytical guess for the beam displacement. The resulting F-D relationship is given by the following equation:

$$F = \left(\frac{\pi^2}{2}\frac{\sigma_0 wh}{L} + \frac{\pi^4}{6}\frac{Ewh^3}{L^3}\right)u + \frac{\pi^4}{8}\frac{Ewh}{L^3}u^3 \approx \left(4.93\frac{\sigma_0 wh}{L} + 16.23\frac{Ewh^3}{L^3}\right)u + 12.17\frac{Ewh}{L^3}u^3, \quad (52)$$

where w and h are the width and thickness of the rectangular beam, respectively. First, it is worth comparing this approximated analytical result with the accurate analytical expansion given by Eqs. (10) and (19), using the rectangular moment of inertia, $I = wh^3/12$. The resulting expansion yields

$$F = \left(\frac{24}{5}\frac{\sigma_0 wh}{L} + 16\frac{Ewh^3}{L^3}\right)u + \frac{288}{25}\frac{Ewh}{L^3}u^3 \approx \left(4.8\frac{\sigma_0 wh}{L} + 16\frac{Ewh^3}{L^3}\right)u + 11.52\frac{Ewh}{L^3}u^3. \quad (53)$$

Equation (52) may naively be considered to be a good approximation of the analytical expansion, Eq. (53). Using a, b, and c to denote the numerical prefactors of the two expansions, from left to right, we find that the relative errors are small: $\delta a/a = (4.93 - 4.8)/4.8 = 0.027$, $\delta b/b = (16.23 - 16)/16 = 0.014$, and $\delta c/c = (12.17 - 11.52)/11.52 = 0.056$. Since these two relationships contain also non-linear terms (u^3), the extracted results from the two models are, however, significantly different. Following is a detailed comparison between these two models.

We first chose typical values for a rectangular SiNW, i.e., E = 190 GPa, $\sigma_0 = 500$ MPa, width w = 40 nm, thickness t = 40 nm, and length L = 1 μm. Then, we obtained the correct F-D curve for these parameters by numerically solving the set of equations for the 3-point bending analysis. This F-D curve is referred to as the experimental data against which three approximate models were tested. Three displacement (u) ranges were examined: (a) small, $u < 3(w/2)$, (b) medium, $u < 6(w/2)$, and (c) large, $u < 10(w/2)$. The three approximate models are described by Eq. (52), f_1 (1st order), and f_4.

Figs. 6(a)–6(c) present the experimental data and the three fitting curves according to Eqs. (52), (19), and (25). Surprisingly, for each displacement range all four curves are almost identical. Such excellent agreement between experimental and theoretical usually leads researchers to assume that their theoretical model is accurate and successful in capturing the correct physics of the problem. In this case, however, the three models are very different from one another. Thus, the extracted Young's modulus and residual stress should be examined for each approximation, and compared with the known values that were chosen originally in order to fabricate this experimental force displacement curve. Figs. 7(a) and 7(b) present the results of such analysis.

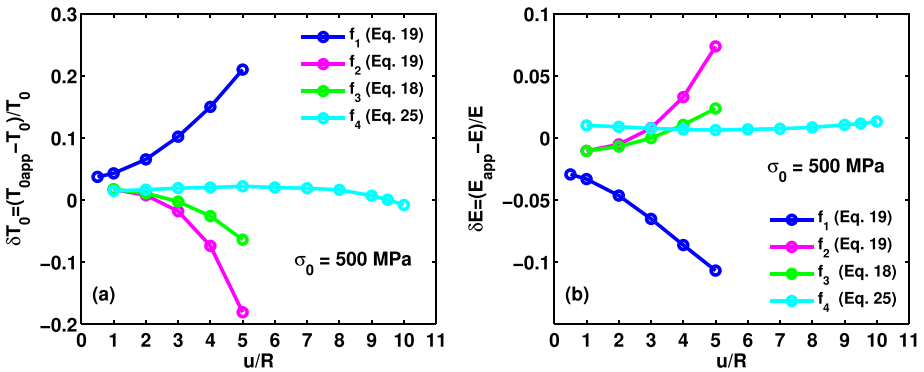

FIG. 5. The relative error in the extracted residual tension (a) and Young's modulus (b) for different fitting ranges measured in beam radius (u/R) for the four listed approximations. The theoretical force-deflection data was calculated with initial stress of $\sigma_0 = 500$ MPa, and Young's modulus of $E = 190$ GPa.

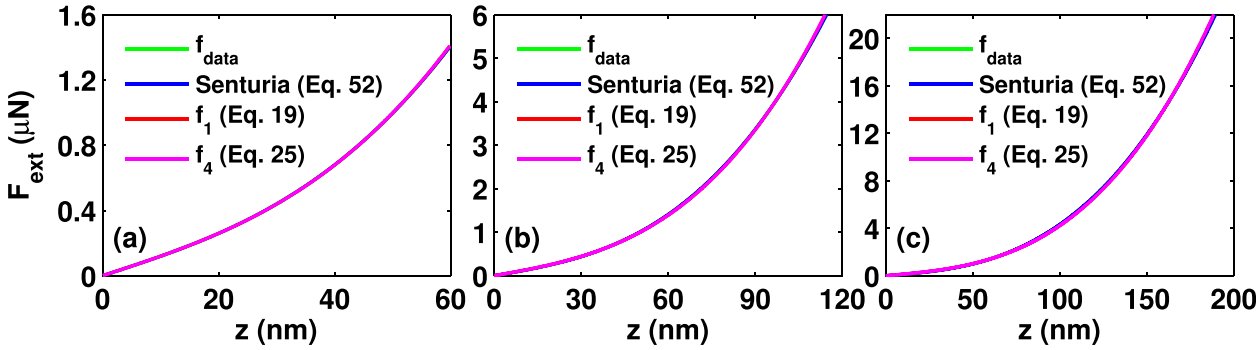

FIG. 6. Experimental F-D curve (green line) and three fitting curves (blue, red, and magenta) according to Eqs. (52), (19), and (25), respectively, for three displacement ranges (a) $u < 3(w/2)$, (b) $u < 6(w/2)$, and (c) $u < 10(w/2)$.

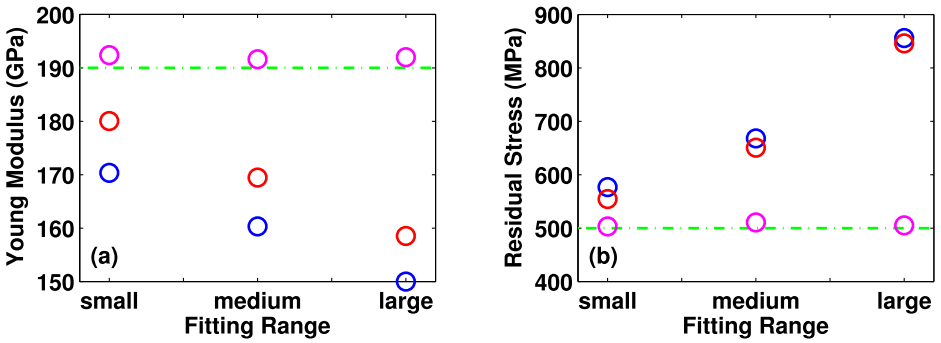

FIG. 7. Theoretical and extracted results according to the previous fitting curves (Fig. 6) for the Young's modulus (a) and residual stress (b). The different fitting ranges are labeled, small, medium, and large and correspond to $u < 3(w/2)$, $u < 6(w/2)$, and $u < 10(w/2)$, respectively. Green dashed lines are theoretical values, blue, red, and magenta circles are results according to Eqs. (52), (19), and (25), respectively.

The green dashed lines in Figs. 7(a) and 7(b) correspond to the chosen values of the Young's modulus and residual stress, i.e., E = 190 GPa and $\sigma_0 = 500$ MPa, respectively, and the blue, red and magenta circles correspond to the extracted values according to Eqs. (52), (19), and (25), respectively. As expected, for the small fitting range, the two approximations f_1 and f_4 yield good estimations for E and σ_0, although approximation f_4 is much better. As the fitting range increases, approximation f_1 deviates increasingly from the theoretical values as opposed to approximation f_4, which remains almost unchanged over the three fitting ranges. This observation is crucial, and the fact that f_4 is "immune" from this phenomenon for large fitting ranges are of substantial importance. The Senturia model is the least accurate, and even for short fitting ranges it yields erroneous results. Nevertheless, it is a very commonly used approximation, not only for SiNWs but also for extracting the Young's modulus and residual stress of other beam-like structures, such as graphene nanoribbons.[49] An alternative approach, which uses the same structure of Eq. (52) but with different prefactors that were calculated numerically using the finite element method, is limited as well.[48] In the best scenario, the prefactors will be identical to the analytical expansion, Eq. (53), and according to Figs. 7(a) and 7(b) the extracted E and σ_0 will be less accurate in comparison with Eq. (25).

To acquire an additional tool for analyzing beam deflections and to confirm the suggested model's validity, finite element (FE) simulations (COMSOL Multiphysics 3.4a) were carried out. Structures comparable in size and expected elastic properties to experimentally measured NW beams were constructed and subjected to a center point load. Fig. 8 shows F-D curves obtained by solving the exact beam equations, namely, Eqs. (10), (11), and (12) (red lines), the polynomial approximation f_4 (light blue dashed lines), and the FE simulations (blue circles), using the same NW parameters. Curves 1, 2, and 3 simulate beams of varying stresses: $\sigma_0 = 0$ MPa, -500 MPa, and 500 MPa, respectively. Curve 4 simulates a longer beam of $L = 2\,\mu$m and $\sigma_0 = -100$ MPa. Note that the stress-free case of curve 1 corresponds to Heidelberg's model. Also note the excellent agreement between the exact solutions, the analytical approximation (with and without initial stress), and the FE simulations.

Equipped with this procedure, beam deflections can be experimentally studied using a 3-point bending apparatus. Results of such experiments and analyses of SiNWs were

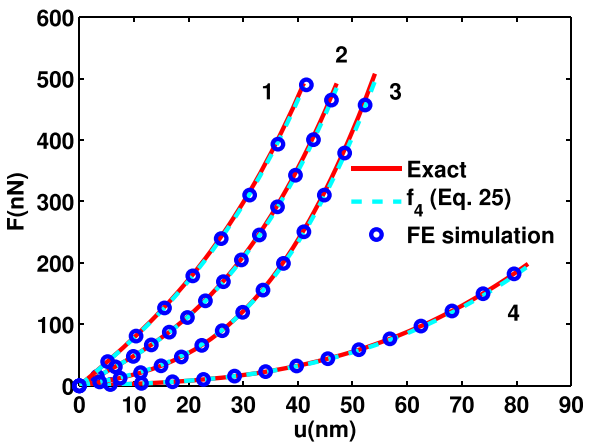

FIG. 8. Force-deflection curves obtained by the exact solution of the beam equations, the polynomial approximation, f_4, and FE simulations. All curves correspond to NW beams of $d = 40$ nm and $E = 190$ GPa. Curves 1, 2, and 3 simulate beams of $L = 1\,\mu$m and $\sigma_0 = 0$ MPa, -500 MPa, and 500 MPa, respectively. Curve 4 simulates a beam of $L = 2\,\mu$m and $\sigma_0 = -100$ MPa.

presented by Calahorra *et al.*[50] In brief, doubly clamped suspended SiNW beams were fabricated in a single e-beam lithography (EBL) step process.[51] Three-point bending experiments were then performed on the suspended beams before and after RTA. Non-oxidized and oxidized SiNWs of two different SiO_2 sheath thickness were tested. Fig. 9 presents the resulting E_{eff} (black circles) for these wires obtained according to the presented theoretical model and approximation f_4. Seven devices contained native oxide ($d_{shell} \approx 2$ nm), and two were oxidized ($d_{shell} \approx 7$ nm). These results were compared with results from the core-shell model introduced by Eq. (2) which offers four relevant possibilities for such NWs: two shell thicknesses (2 nm and 7 nm) and two expected core Young's moduli, E_{core} ($E_{\langle 110\rangle,\langle 112\rangle} = 170$ GPa and $E_{\langle 111\rangle} = 190$ GPa). The blue and light blue curves correspond to non-oxidized SiNWs with $E_{core} = 170$ GPa and 190 GPa, respectively, and the red and magenta lines represent oxidized wires with $E_{core} = 170$ GPa and 190 GPa, respectively. Note that the good agreement between the theoretical model and the measured data as well as the dependence of E_{eff} on NW diameter, as predicted. This result suggests that for narrow SiNWs with core diameters greater than 20 nm, the decrease in the effective Young's modulus with wire diameter is not related to the nanosize effect, as several studies previously predicted,[41,52] but is fully explained within the core-shell model (Eq. (2)).

Figs. 10(a) and 10(b) present plots of the resulting σ_0 and E_{core} vs. NW diameter. Fig. 10(b) shows the ratios of extracted E_{core} to the theoretical Young's modulus according to the wire's crystallographic growth orientation. Red circles correspond to $E_{core}/(E_{\langle 110\rangle,\langle 112\rangle} = 170$ GPa) and blue circles represent $E_{core}/(E_{\langle 111\rangle} = 190$ GPa). The experimental data are scattered nicely around 1, and the average Young's moduli obtained from these devices are 169 ± 10 GPa (red data) and 194 ± 12 GPa (blue data). These extracted Young's moduli are in excellent agreement with bulk Si with $\langle 110\rangle$, or $\langle 112\rangle$, and $\langle 111\rangle$ crystallographic growth orientations ($E_{\langle 110\rangle,\langle 112\rangle} = 170$ GPa and $E_{\langle 111\rangle} = 190$ GPa), which is expected considering the NWs used.[53] Interestingly, the residual stress for these NWs, as shown in Fig. 10(a), ranges between −30 MPa and 450 MPa, with no obvious correlation between the NW diameters and the stress.

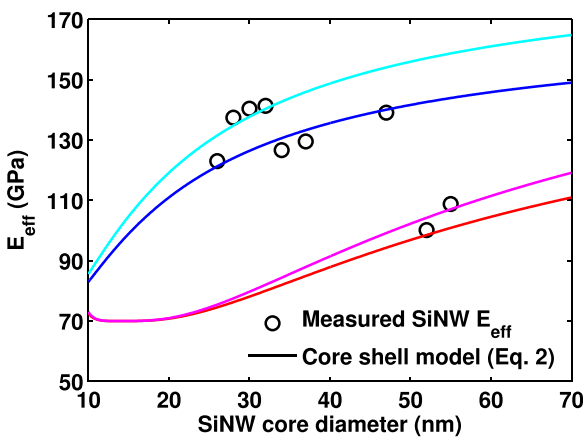

FIG. 9. The core-shell model prediction for $E_{core} = 170$ GPa or 190 GPa and shell thickness of 2 nm or 7 nm (colored lines, see main text) alongside the extracted fitting results for the effective Young's modulus (black circles).

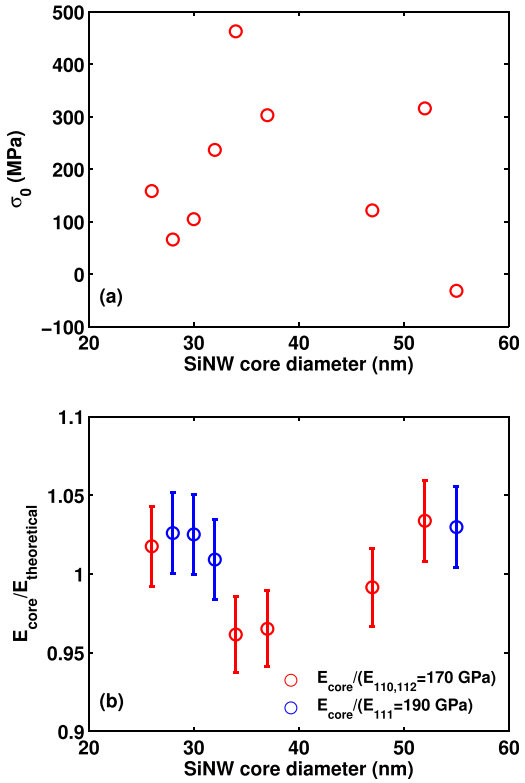

FIG. 10. (a) The extracted residual stress, σ_0, vs. nanowire diameter. (b) The extracted E_{core} divided by the expected theoretical Young's modulus (red circles for $E_{\langle 110\rangle,\langle 112\rangle} = 170$ GPa and blue circles for $E_{\langle 111\rangle} = 190$ GPa) vs. nanowire diameter.

The possibility of fine-tuning the residual stresses of electronic devices is of great importance, and to that end we also studied the origin of the stresses we obtained. First, we verified that the source of residual tension is not related to the adsorption of adatoms on the wire's circumference by conducting our 3-point bending experiments with and without treatment with ozone plasma and obtained similar results. Ozone plasma removes any residues and contaminations that may adhere to the nanowire during its fabrication process. The fact that the results were similar rules out the possibility of such surface residue and/or contamination. Etching cannot be responsible either, since no etching takes place during the fabrication process. Deposition happens only on the source and drain electrodes and, indeed, we have evidence that the shape and structure of these electrodes may affect the resulting stresses and may modify them in a controlled manner. For configurations in which several thin rectangular electrodes are deposited on the nanowire adjacent to one another, the suspended segment remains parallel to the wafer substrate and the residual stresses remain small. If, however, the source and drain electrodes are wide and far from any other electrodes, the resulting stresses are greater than before. Yet, the main process that modifies residual stresses is attributed to RTA, as presented below.

During RTA, nickel silicide segments are formed adjacent to the Ni source and drain electrodes and compressive strains are observed along the SiNW.[20,54,55] Hence, devices

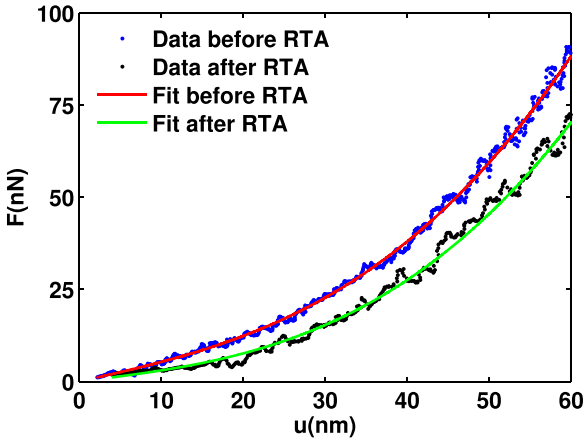

FIG. 11. Measured F-D curve (blue and black dots) and fitting curves (red and green lines) for a SiNW of $d = 26$ nm, $L = 1.35\,\mu$m, before and after RTA at 400° C. Fitting results before RTA - $E_{eff} = 123$ GPa and $\sigma_0 = 159$ MPa, and after RTA - $E_{eff} = 113$ GPa and $\sigma_0 = 45$ MPa.

are expected to have smaller initial stress values after RTA; indeed, values may even be negative.

Fig. 11 shows measured F-D curves taken from the same device before and after RTA at 400° C for 30 s. The geometric parameters are $L = 1.35\,\mu$m and $d = 26$ nm for both cases. Fitting results were based on the f_4 approximation. Fitting results before RTA are $E_{eff} = 123$ GPa, and $\sigma_0 = 159$ MPa which corresponds to $E_{core} = 173$ GPa (Eq. (2)), while after RTA $E_{eff} = 113$ GPa, and $\sigma_0 = 45$ MPa, yielding $E_{core} = 154$ GPa. After RTA, E_{eff} is smaller since the Young's modulus for NiSi is smaller than that for Si (reported to be about 130 GPa (Ref. 56)), and because parts of the SiNW turn into NiSi after RTA. A significant change of about -115 MPa in the initial stress was found, corresponding to compression during RTA.

Alternatively, we may examine the modification of the residual stresses due to the formation of nickel silicide phases near the source and drain contacts. Previous studies have established that a nickel-rich phase is formed near the nickel contacts. The transformation $2Ni + \mathrm{Si} \rightleftarrows \mathrm{Ni_2Si}$ usually takes place, and the atomic volume along the wire changes. The relative change in atomic volume depends on the specific Ni_2Si phase that is formed near the contacts. However, the atomic volume of Ni_2Si is, to a good approximation, $V_{Ni_2Si} = 33\,\text{Å}^3$, where $V_{SiNW} = 20\,\text{Å}^3$ for SiNW. Thus, the relative change of volume is $\frac{\delta V}{V} = \frac{13}{20}$, and along the wire it is $\frac{\delta l}{l} \approx 0.2$. Although not all the NW segment transforms into nickel-rich silicide, we concluded from SEM images that a small fraction near the two anchoring points, of several nm up to about ten nm, was transformed into a nickel-rich phase. Hence, the expected stress modification may be as large as 400 MPa and it always reduces the initial stress, σ_0. The initial stress may be positive but small, and as a result of the RTA, the relaxed length of the wire increases, thus reducing the built-in stress of the remaining silicon segment. If the amount of nickel-rich silicide is large enough (1% of the entire NW), the positive stress will change sign, indicating that the wire is under compression; if it exceeds the Euler-Bernoulli instability criteria for buckling, the NW will bend, as we found experimentally in some of our NWs.

These two examples emphasize the importance of including the residual stresses in the 3-point bending analysis, and stress the significance of the optimal approximation, f_4, in extracting the correct Young's moduli, including the NW's growth orientation.

VI. SUMMARY

In conclusion, we introduce a comprehensive model for the 3-point bending experiment of doubly clamped beams in which initial stresses of elongation or compression are present along the beam. We offer a self-consistent solution for the set of beam equations and develop and compare several approximations with the exact numerical results. The quality and validity range of each approximation were studied, and a novel approximation, named f_4 (Eq. (25)), was found to be significantly better than others. The model and the best approximation were compared with FE simulations and were found to be in remarkable agreement.

A theoretical analysis of the model showed the importance of including initial stresses in the analysis of the mechanical properties of suspended NWs. Ignoring them may lead to large errors in determining Young's modulus, especially when applying the linear model to the force-displacement curve.

Two examples of 3-point bending experiments were presented, and a theoretical analysis was used to determine the correct Young's moduli, the residual stresses, and the crystallographic growth orientations of the tested NWs. The analysis confirms that RTA causes compression along the SiNW beams and that the core-shell model is applicable for describing the elastic properties of SiNWs with beam diameters greater than 20 nm. This procedure is not restricted to SiNW beams, but may be used on a large variety of doubly clamped suspended beams that undergo 3-point bending analysis.

ACKNOWLEDGMENTS

The authors thank the Russell Berrie Nanotechnology Institute, the Micro Nano Fabrication Unit at the Technion, and the Israeli Ministry of Industry, Trade and Labor via the MAGNET program (ALPHA Consortium) for their support.

[1]Y. Li, F. Qian, J. Xiang, and C. M. Lieber, Mater. Today **9**, 18 (2006).
[2]P. J. Pauzauskie and P. Yang, Mater. Today **9**, 36 (2006).
[3]C. Thelander, P. Agarwal, S. Brongersma, J. Eymery, L. Feiner, A. Forchel, M. Scheffler, W. Riess, B. Ohlsson, U. Gsele, and L. Samuelson, Mater. Today **9**, 28 (2006).
[4]Y. Cui, Z. Zhong, D. Wang, W. U. Wang, and C. M. Lieber, Nano Lett. **3**, 149 (2003).
[5]G. Zheng, W. Lu, S. Jin, and C. M. Lieber, Adv. Mater. **16**, 1890 (2004).
[6]D. Kim, Y. Jung, M. Park, B. Kim, S. Hong, M. Choi, M. Kang, Y. Yu, D. Whang, and S. Hwang, IEEE Trans. Nanotechnol. **7**, 683 (2008).
[7]X. Duan, Y. Huang, R. Agarwal, and C. M. Lieber, Nature **421**, 241 (2003).
[8]X. L. Feng, R. He, P. Yang, and M. L. Roukes, Nano Lett. **7**, 1953 (2007).
[9]Q. Li, S.-M. Koo, C. Richter, M. Edelstein, J. Bonevich, J. Kopanski, J. Suehle, and E. Vogel, IEEE Trans. Nanotechnol. **6**, 256 (2007).
[10]M. Li, R. B. Bhiladvala, T. J. Morrow, J. A. Sioss, K.-K. Lew, J. M. Redwing, C. D. Keating, and T. S. Mayer, Nat. Nanotechnol. **3**, 88 (2008).
[11]Y. Cui, Q. Wei, H. Park, and C. M. Lieber, Science **293**, 1289 (2001).
[12]K. S. Kim, H.-S. Lee, J.-A. Yang, M.-H. Jo, and S. K. Hahn, Nanotechnology **20**, 235501 (2009).

[13]Y. L. Bunimovich, Y. S. Shin, W.-S. Yeo, M. Amori, G. Kwong, and J. R. Heath, J. Am. Chem. Soc. **128**, 16323 (2006).
[14]R. He and P. Yang, Nat. Nanotechnol. **1**, 42 (2006).
[15]S. Thompson, G. Sun, Y. S. Choi, and T. Nishida, IEEE Trans. Electron Devices **53**, 1010 (2006).
[16]X. F. Fan, L. F. Register, B. Winstead, M. C. Foisy, W. Chen, X. Zheng, B. Ghosh, and S. K. Banerjee, IEEE Trans. Electron Devices **54**, 291 (2007).
[17]W. Chang and J. Lin, Microelectron. Eng. **86**, 1965 (2009).
[18]M.-F. Yu, O. Lourie, M. J. Dyer, K. Moloni, T. F. Kelly, and R. S. Ruoff, Science **287**, 637 (2000).
[19]S. Hoffmann, I. Utke, B. Moser, J. Michler, S. H. Christiansen, V. Schmidt, S. Senz, P. Werner, U. Gosele, and C. Ballif, Nano Lett. **6**, 622 (2006).
[20]K.-C. Lu, W.-W. Wu, H.-W. Wu, C. M. Tanner, J. P. Chang, L. J. Chen, and K. N. Tu, Nano Lett. **7**, 2389 (2007).
[21]C.-L. Hsin, W. Mai, Y. Gu, Y. Gao, C.-T. Huang, Y. Liu, L.-J. Chen, and Z.-L. Wang, Adv. Mater. **20**, 3919 (2008).
[22]Y. Zhu, F. Xu, Q. Qin, W. Fung, and W. Lu, Nano Lett. **9**, 3934 (2009).
[23]F. Xu, W. Lu, and Y. Zhu, ACS Nano **5**(1), 672 (2011).
[24]D. A. Smith, V. C. Holmberg, and B. A. Korgel, ACS Nano **4**(4), 2356 (2010).
[25]X. Li, H. Gao, C. J. Murphy, and K. K. Caswell, Nano Lett. **3**, 1495 (2003).
[26]M. Riaz, O. Nur, M. Willander, and P. Klason, Appl. Phys. Lett. **92**, 103118 (2008).
[27]M. Tabib-Azar, M. Nassirou, R. Wang, S. Sharma, T. I. Kamins, M. S. Islam, and R. S. Williams, Appl. Phys. Lett. **87**, 113102 (2005).
[28]E. W. Wong, P. E. Sheehan, and C. M. Lieber, Science **277**, 1971 (1997).
[29]A. Heidelberg, L. T. Ngo, B. Wu, M. A. Phillips, S. Sharma, T. I. Kamins, J. E. Sader, and J. J. Boland, Nano Lett. **6**, 1101 (2006).
[30]A. S. Paulo, J. Bokor, R. T. Howe, R. He, P. Yang, D. Gao, C. Carraro, and R. Maboudian, Appl. Phys. Lett. **87**, 053111 (2005).
[31]B. Wu, A. Heidelberg, and J. J. Boland, Nat. Mater. **4**, 525 (2005).
[32]L. T. Ngo, D. Almecija, J. E. Sader, B. Daly, N. Petkov, J. D. Holmes, D. Erts, and J. J. Boland, Nano Lett. **6**, 2964 (2006).
[33]G. Y. Jing, H. L. Duan, X. M. Sun, Z. S. Zhang, J. Xu, Y. D. Li, J. X. Wang, and D. P. Yu, Phys. Rev. B **73**, 235409 (2006).
[34]Q. Xiong, N. Duarte, S. Tadigadapa, and P. C. Eklund, Nano Lett. **6**, 1904 (2006).
[35]B. Varghese, Y. Zhang, L. Dai, V. B. C. Tan, C. T. Lim, and C.-H. Sow, Nano Lett. **8**, 3226 (2008).
[36]H. Ni, X. Li, and H. Gao, Appl. Phys. Lett. **88**, 043108 (2006).
[37]B. Wen, J. E. Sader, and J. J. Boland, Phys. Rev. Lett. **101**, 175502 (2008).
[38]D. Almecija, D. Blond, J. E. Sader, J. N. Coleman, and J. J. Boland, Carbon **47**, 2253 (2009).
[39]H. Sadeghian, C. K. Yang, J. F. L. Goosen, E. van der Drift, A. Bossche, P. J. French, and F. van Keulen, Appl. Phys. Lett. **94**, 221903 (2009).
[40]X. Li, T. Ono, Y. Wang, and M. Esashi, Appl. Phys. Lett. **83**, 3081 (2003).
[41]B. Lee and R. E. Rudd, Phys. Rev. B **75**, 041305 (2007).
[42]P. W. Leu, A. Svizhenko, and K. Cho, Phys. Rev. B **77**, 235305 (2008).
[43]L. Ma, J. Wang, J. Zhao, and G. Wang, Chem. Phys. Lett. **452**, 183 (2008).
[44]J. He and C. M. Lilley, Nano Lett. **8**, 1798 (2008).
[45]C. Q. Chen, Y. Shi, Y. S. Zhang, J. Zhu, and Y. J. Yan, Phys. Rev. Lett. **96**, 075505 (2006).
[46]M. J. Gordon, T. Baron, F. Dhalluin, P. Gentile, and P. Ferret, Nano Lett. **9**, 525 (2009).
[47]L. Landau and E. Lifshitz, *Theory of Elasticity*, 3rd ed. (Pergamon Press, 1986).
[48]S. D. Senturia, *Microsystem Design* (Kluwer Academic Publishing, 2001).
[49]I. W. Frank, D. M. Tanenbaum, A. M. Van der Zande, and P. L. McEuen, J. Vac. Sci. Technol., B **25**, 2558 (2007).
[50]Y. Calahorra, O. Shtempluck, V. Kotchtakov, and Y. E. Yaish, "Young's modulus, residual stress, and crystal orientation of doubly clamped silicon nanowire beams," Nano. Lett. (published online).
[51]O. Shirak, O. Shtempluck, V. Kotchtakov, G. Bahir, and Y. Yaish, Nanotechnology **23**, 395202 (2012).
[52]H. Yu, C. Sun, W. Zhang, S. Lei, and Q. Huang, J. Nanomater. **2013**, 319302 (2013).
[53]According to SiNWs supplier, growth wafers bear SiNWs of $\langle 110\rangle$, $\langle 112\rangle$, $\langle 111\rangle$ directions. Anisotropic crystals have different Young's modulus in different directions given by $\frac{1}{E} = S_{11} - 2\left(S_{11} - S_{12} - \frac{1}{2}S_{44}\right)\left(\ell_1^2\ell_2^2 + \ell_2^2\ell_3^2 + \ell_1^2\ell_3^2\right)$,[48] where (ℓ_1, ℓ_2, ℓ_2) are the directional cosines of the crystal direction. Yielding $E_{110} = E_{112} = 170$ GPa, and $E_{111} = 190$ GPa.
[54]E. Y. Yaish, A. Katsman, G. M. Cohen, and M. Beregovsky, J. Appl. Phys. **109**, 094303 (2011).
[55]M. J. Beregovsky, A. Katsman, E. M. Hajaj, and E. Y. Yaish, Solid-State Electron. **80**, 110 (2013).
[56]M. Qin and V. M. C. Poon, J. Mater. Sci. Lett. **19**, 2243 (2000).